



# Ultralow thermal conductivity in all-inorganic halide perovskites

Woochul Lee<sup>a,b,1</sup>, Huashan Li<sup>c,1</sup>, Andrew B. Wong<sup>a,d,1</sup>, Dandan Zhang<sup>a,d</sup>, Minliang Lai<sup>a</sup>, Yi Yu<sup>a,d</sup>, Qiao Kong<sup>a</sup>, Elbert Lin<sup>a</sup>, Jeffrey J. Urban<sup>b</sup>, Jeffrey C. Grossman<sup>c</sup>, and Peidong Yang<sup>a,d,e,f,2</sup>

<sup>a</sup>Department of Chemistry, University of California, Berkeley, CA 94720; <sup>b</sup>Molecular Foundry, Lawrence Berkeley National Laboratory, Berkeley, CA 94720;

<sup>c</sup>Department of Materials Science and Engineering, Massachusetts Institute of Technology, Cambridge, MA 02139; <sup>d</sup>Materials Sciences Division, Lawrence Berkeley National Laboratory, Berkeley, CA 94720; <sup>e</sup>Department of Materials Science and Engineering, University of California, Berkeley, CA 94720; and <sup>f</sup>Kavli Energy NanoScience Institute, Berkeley, CA 94720

Contributed by Peidong Yang, July 8, 2017 (sent for review May 13, 2017; reviewed by Philip Kim and Zhifeng Ren)

**Controlling the flow of thermal energy is crucial to numerous applications ranging from microelectronic devices to energy storage and energy conversion devices. Here, we report ultralow lattice thermal conductivities of solution-synthesized, single-crystalline all-inorganic halide perovskite nanowires composed of  $\text{CsPbI}_3$  ( $0.45 \pm 0.05 \text{ W}\cdot\text{m}^{-1}\cdot\text{K}^{-1}$ ),  $\text{CsPbBr}_3$  ( $0.42 \pm 0.04 \text{ W}\cdot\text{m}^{-1}\cdot\text{K}^{-1}$ ), and  $\text{CsSnI}_3$  ( $0.38 \pm 0.04 \text{ W}\cdot\text{m}^{-1}\cdot\text{K}^{-1}$ ). We attribute this ultralow thermal conductivity to the cluster rattling mechanism, wherein strong optical-acoustic phonon scatterings are driven by a mixture of 0D/1D/2D collective motions. Remarkably,  $\text{CsSnI}_3$  possesses a rare combination of ultralow thermal conductivity, high electrical conductivity ( $282 \text{ S}\cdot\text{cm}^{-1}$ ), and high hole mobility ( $394 \text{ cm}^2\cdot\text{V}^{-1}\cdot\text{s}^{-1}$ ). The unique thermal transport properties in all-inorganic halide perovskites hold promise for diverse applications such as phononic and thermoelectric devices. Furthermore, the insights obtained from this work suggest an opportunity to discover low thermal conductivity materials among unexplored inorganic crystals beyond caged and layered structures.**

halide perovskite | thermal conductivity | thermal transport | nanowire | thermoelectrics

**M**anipulation and utilization of thermal energy can be revolutionized via the discovery of novel materials with extreme thermal transport properties (1). Materials with low thermal conductivity are sought for turbine engines, thermal data storage devices, and thermoelectric energy conversion devices (2–4), and materials with high thermal conductivity are required to dissipate heat efficiently from microelectronic devices (5). While electrically insulating amorphous solids generally possess the lowest thermal conductivities (6), single crystals with ultralow thermal conductivity are rare due to their well-ordered atomic structure, and these rare crystals often involve complicated compositions and expensive synthetic processes (4, 7). To achieve low thermal conductivity, complex systems have been designed with large numbers of atoms in the primitive unit cell along with cage-like crystal structures that exhibit atomic rattling motions (e.g., skutterudites and clathrates) (8, 9). Other approaches use disordered layer structures and superlattice structures. For example, the thermal conductivity in disordered layered crystals of  $\text{WSe}_2$  was found to be lower than the amorphous limit in the cross-plane direction (10), and the thermal conductivity of epitaxial oxide superlattices was reduced below the alloy limit by phonon interference effects (11). However, finding materials with low thermal conductivity in a simple, fully dense, and single-crystalline solid with a simple synthetic process has proven extremely challenging.

Halide perovskite materials have attracted significant attention for their excellent optoelectronic properties. This family of materials spans organic-inorganic hybrid halide perovskites (HHP) such as  $\text{CH}_3\text{NH}_3\text{BX}_3$  and  $\text{HC}(\text{NH}_2)_2\text{BX}_3$  as well as all-inorganic halide perovskites (AIHP), which include  $\text{CsBX}_3$  (where  $B = \text{Pb}, \text{Sn}$  and  $X = \text{Cl}, \text{Br}, \text{I}$ ). Both of these halide perovskites have been investigated for potential applications in solution-processed optoelectronic devices

such as photovoltaics (12, 13), light-emitting diodes (14, 15), and lasers (16, 17). However, fundamental study of thermal transport in halide perovskites has been significantly lacking despite its practical and fundamental importance. For HHP, very few experimental studies have been performed for thermal conductivity (18, 19) and an ultralow thermal conductivity value of  $0.5 \text{ W}\cdot\text{m}^{-1}\cdot\text{K}^{-1}$  has been reported for single-crystalline  $\text{CH}_3\text{NH}_3\text{PbI}_3$ . Computational study revealed that the main reason for the ultralow thermal conductivity of HHP is rotational motions of organic  $\text{CH}_3\text{NH}_3^+$  ions (20–22). For instance, Hata et al. computationally demonstrated the critical role of  $\text{CH}_3\text{NH}_3^+$  rotations by comparing results with A-site cations possessing different degrees of freedom, where the elimination of the rotational degree of freedom results in greater thermal conductivity by a factor of  $\sim 2$  (20). While limited investigations of thermal transport in HHP have been reported and some aspects of thermal transport in HHP are understood, fundamental understanding of thermal transport in AIHP remains largely elusive. The thermal transport mechanism in AIHP is expected to be fundamentally different from that in HHP, since vibrational density of states in organic and inorganic ions are largely mismatched for HHP, and monoatomic  $\text{Cs}^+$  in AIHP does not contain rotational modes in contrast to the  $\text{CH}_3\text{NH}_3^+$  ion in HHP (20, 21).

Here, we synthesize AIHP  $\text{CsPbI}_3$ ,  $\text{CsPbBr}_3$ , and  $\text{CsSnI}_3$  nanowires (NWs) via solution processes, measure their ultralow thermal conductivity, and elucidate fundamental thermal

## Significance

**Discovery of materials with low thermal conductivity in simple, fully dense, and single-crystalline solids has proven extremely challenging. This paper reports the discovery of ultralow thermal conductivity ( $\sim 0.4 \text{ W}\cdot\text{m}^{-1}\cdot\text{K}^{-1}$ ) in single-crystalline, all-inorganic halide perovskite nanowires, which is comparable to their amorphous limit value. We attribute ultralow thermal conductivity to a cluster rattling mechanism, based on strong phonon-phonon scattering via the coexistence of collective motions involving various atom groups. These results call attention to the vital thermal transport processes and thermal management strategies for applications with all-inorganic halide perovskites. Further,  $\text{CsSnI}_3$  shows a rare combination of ultralow thermal conductivity and high electrical conductivity, so it can be a promising material for unique applications as an electrically conductive thermal insulator.**

Author contributions: W.L., H.L., A.B.W., and P.Y. designed research; W.L., H.L., A.B.W., D.Z., M.L., Y.Y., Q.K., and E.L. performed research; W.L., H.L., and A.B.W. analyzed data; and W.L., H.L., A.B.W., J.J.U., J.C.G., and P.Y. wrote the paper.

Reviewers: P.K., Harvard University; and Z.R., University of Houston.

The authors declare no conflict of interest.

<sup>1</sup>W.L., H.L., and A.B.W. contributed equally to this work.

<sup>2</sup>To whom correspondence should be addressed. Email: p\_yang@berkeley.edu.

This article contains supporting information online at [www.pnas.org/lookup/suppl/doi:10.1073/pnas.1711744114/-DCSupplemental](http://www.pnas.org/lookup/suppl/doi:10.1073/pnas.1711744114/-DCSupplemental).

transport in AIHP. Whereas we have developed solution-phase synthetic methods for  $\text{CsPbI}_3$  and  $\text{CsPbBr}_3$  NWs (17, 23) (details in *SI Appendix*), we report the successful low-temperature solution-phase synthesis of black orthorhombic phase  $\text{CsSnI}_3$  ( $\text{B}-\text{CsSnI}_3$ ) NWs in this work (*SI Appendix*, Figs. S1 and S4), which has been a challenge because of the tendency to form a more stable yellow polymorph of  $\text{CsSnI}_3$  based on  $[\text{Sn}_2\text{I}_6^{2-}]$  double chains (24, 25). The  $\text{B}-\text{CsSnI}_3$  has a direct bandgap of 1.3 eV, and unlike other materials with strong emission in the near-infrared, this material does not contain toxic lead or cadmium or require highly reactive metal-organic chemical vapor deposition precursors (24). We confirmed  $\text{B}-\text{CsSnI}_3$  by X-ray powder diffraction and single-NW photoluminescence (*SI Appendix*, Fig. S2).

At room temperature,  $\text{CsPbI}_3$  NWs adopt a double-chain structure in the orthorhombic  $\text{Pnma}$  space group ( $\delta$ ) while  $\text{CsPbBr}_3$  and  $\text{B}-\text{CsSnI}_3$  NWs have a distorted perovskite phase in the orthorhombic  $\text{Pbnm}$  space group ( $\gamma$ ) (Fig. 1 A–C). Although  $\delta-\text{CsPbI}_3$  does not possess the 3D bonding network characteristic of the perovskite structure, we investigate  $\delta-\text{CsPbI}_3$  along with  $\gamma-\text{CsPbBr}_3$  and  $\gamma-\text{CsSnI}_3$  as this is a perovskite-related material (see *SI Appendix* for more details). In addition, the distinct connectivity patterns within these materials composed of similar chemical elements provide a desirable platform for understanding the impact of the topological character of the bonding network on thermal transport properties. High-resolution transmission electron microscopy, fast Fourier transforms of the lattice images, and selected area electron diffraction data for  $\text{CsPbI}_3$ ,  $\text{CsPbBr}_3$ , and  $\text{CsSnI}_3$  NWs confirm that these NWs are single crystalline, and that the crystal growth directions are [010], [110], and [110], respectively (Fig. 1 D–F and *SI Appendix*, Fig. S3). The difference of crystal growth direction in  $\text{CsPbI}_3$  NWs resulted from the different crystal structure as described above.

To measure the thermal conductivity along the length of the AIHP NWs, we used suspended microisland devices (Fig. 1 G–I) (26). We validated the experimental platform by measuring the thermal conductivity of amorphous  $\text{SiO}_2$  NWs (*SI Appendix*, Fig. S5). Further, we estimated the thermal contact resistance between the AIHP NWs and Pt electrodes, and the contact resistance is found to be ~3% of the intrinsic thermal resistance of the AIHP NWs (*SI Appendix*, Fig. S6).

The measured temperature-dependent thermal conductivity for a representative NW of each composition is presented in Fig. 2. The characteristic lengths of the NWs, which can be represented in terms of the Casimir length ( $\sqrt{4wh/\pi}$ , where  $w$  is the width and  $h$  is the height) (27), are 134, 240, and 400 nm for  $\text{CsPbI}_3$ ,  $\text{CsPbBr}_3$ , and  $\text{CsSnI}_3$ , respectively. To obtain the lattice thermal conductivity ( $k_{\text{lattice}}$ ) from the measured total thermal conductivity ( $k_{\text{total}}$ ) in  $\text{CsSnI}_3$ , we directly measured electrical conductivity (details are described below and in *SI Appendix*) and estimated electronic thermal conductivity ( $k_{\text{electron}}$ ) from the Wiedemann-Franz law. Subsequently,  $k_{\text{lattice}}$  is obtained by subtracting  $k_{\text{electron}}$  from  $k_{\text{total}}$  ( $k_{\text{lattice}} = k_{\text{total}} - k_{\text{electron}}$ ). In contrast to  $\text{CsSnI}_3$ , measured thermal conductivity in  $\text{CsPbI}_3$  and  $\text{CsPbBr}_3$  is  $k_{\text{lattice}}$ , since these NWs are electrically insulating (*SI Appendix*). Despite their different compositions and phases,  $k_{\text{lattice}}$  of AIHP NWs is found to be ultralow:  $0.45 \pm 0.05 \text{ W}\cdot\text{m}^{-1}\cdot\text{K}^{-1}$  for  $\text{CsPbI}_3$ ,  $0.42 \pm 0.04 \text{ W}\cdot\text{m}^{-1}\cdot\text{K}^{-1}$  for  $\text{CsPbBr}_3$ , and  $0.38 \pm 0.04 \text{ W}\cdot\text{m}^{-1}\cdot\text{K}^{-1}$  for  $\text{CsSnI}_3$  at room temperature. Further, while amorphous-like thermal transport behaviors are observed in several crystalline materials with low thermal conductivity (28, 29), AIHP NWs exhibit crystal-like thermal conductivity in which the  $k_{\text{lattice}}$  initially increases and then decreases as temperature rises.

To benchmark the observed ultralow  $k_{\text{lattice}}$  of single-crystalline AIHP NWs, we estimated the amorphous limit of  $k_{\text{lattice}}$  ( $k_{\text{min}}$ ) using the model developed by Cahill et al. (6). As can be clearly seen in Fig. 2 A–C,  $k_{\text{lattice}}$  approaches  $k_{\text{min}}$  near room temperature in all AIHP NWs. To verify our experimental results, we measured the thermal conductivity of several single NWs of each composition and confirmed consistent results (*SI Appendix*, Fig. S8). Given the ultralow  $k_{\text{lattice}}$  in single-crystalline AIHP NWs, it is worth comparing with other classes of single-crystalline materials with ultralow thermal conductivity (Fig. 2D). Remarkably,  $k_{\text{lattice}}$  of AIHP NWs are comparable to and even smaller than various crystals such as Zintl compounds, clathrates, and skutterudites (4). Further, the ratio of  $k_{\text{lattice}}$  to  $k_{\text{min}}$  of AIHP NWs at room temperature is only ~2 for all cases (Fig. 2D, Inset). This ratio is lower than that of other crystals exhibiting low thermal conductivity (*SI Appendix*, Table S1), particularly for  $\text{CsPbBr}_3$  and  $\text{CsSnI}_3$ . We also note that AIHP NWs have far smaller thermal conductivity compared with traditional inorganic oxide perovskites whose values are 2–10  $\text{W}\cdot\text{m}^{-1}\cdot\text{K}^{-1}$  (30).

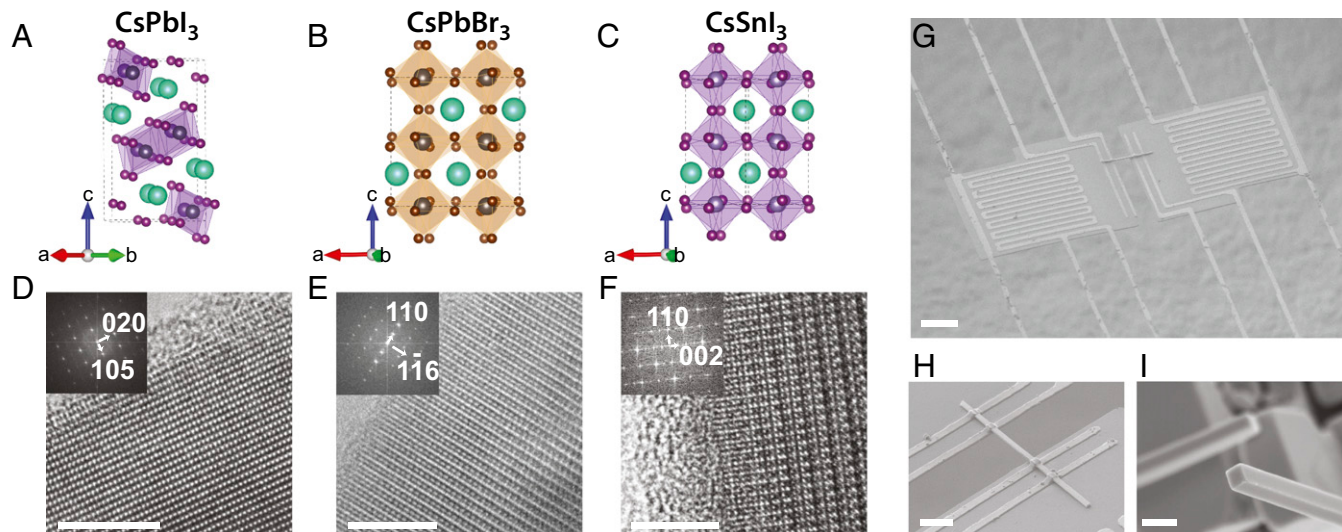


**Fig. 1.** AIHP NWs and suspended microisland devices to measure their thermal and electrical properties. (A–C) Crystal structures of  $\text{CsPbI}_3$ ,  $\text{CsPbBr}_3$ , and  $\text{CsSnI}_3$ . Atoms are colored by Cs: green, Pb: gray, I: purple, Sn: light purple, Br: brown. (D–F) High-resolution transmission electron microscopy images and corresponding fast Fourier transform patterns of  $\text{CsPbI}_3$  (D),  $\text{CsPbBr}_3$  (E), and  $\text{CsSnI}_3$  (F) demonstrate the single-crystalline nature of the AIHP NWs. (G and H) SEM images of suspended microisland devices. Individual AIHP NW is suspended between two membranes. The transport measurement direction is along the growth direction of the NWs. (I) SEM image of the individual AIHP NW. (Scale bars in D–F, 5 nm; in G, 10  $\mu\text{m}$ ; in H, 3  $\mu\text{m}$ ; in I, 1  $\mu\text{m}$ .)

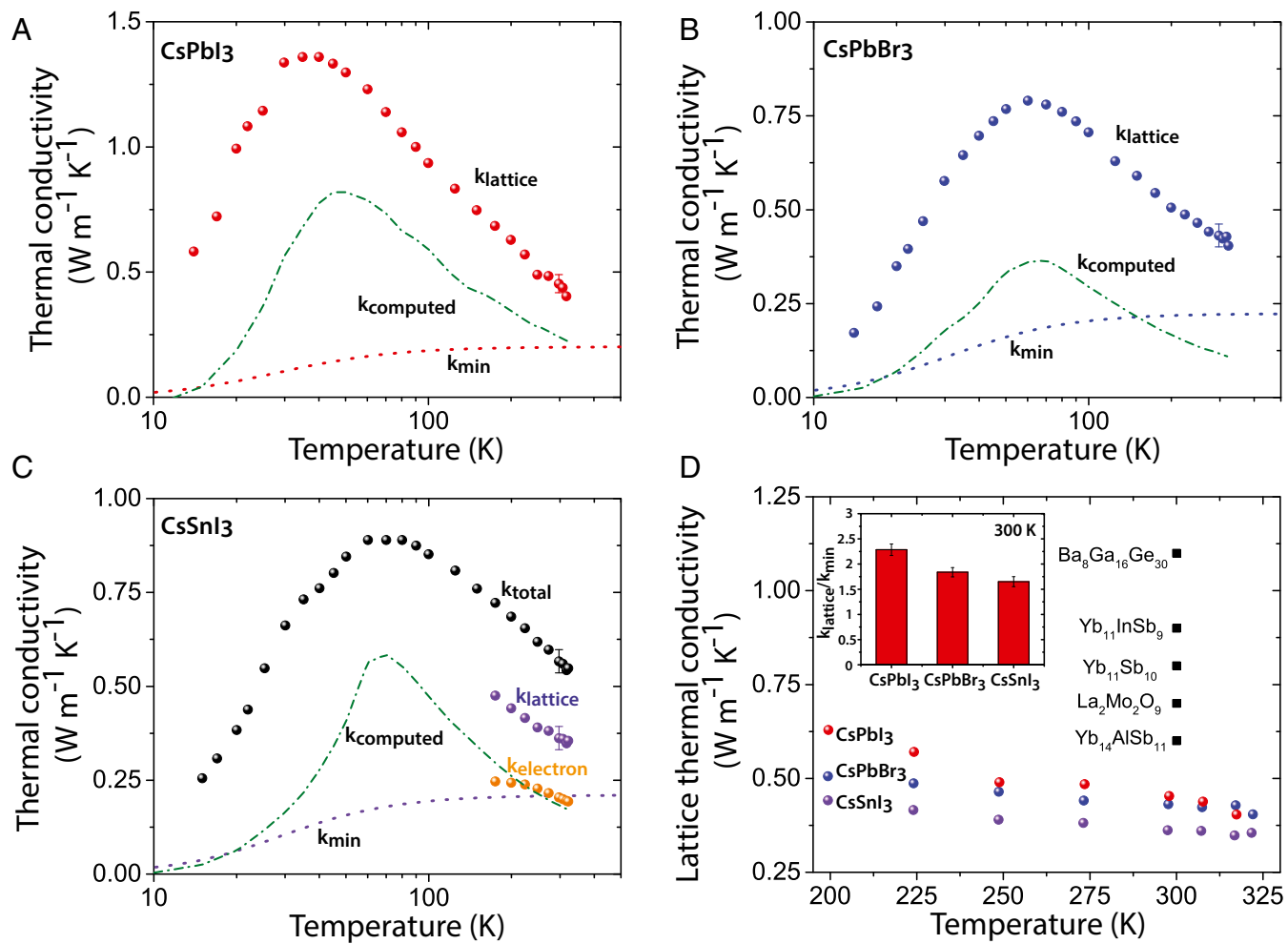


**Fig. 2.** Thermal conductivity of AIHP NWs. (A–C) Measured thermal conductivity ( $k_{\text{lattice}}$  for A and B, and  $k_{\text{total}}$  for C), ab initio calculated lattice thermal conductivity ( $k_{\text{computed}}$ ), and estimated minimum thermal conductivity ( $k_{\text{min}}$ ) for each NW. Electronic thermal conductivity ( $k_{\text{electron}}$ ) for CsSnI<sub>3</sub> NW is estimated from measured electrical conductivity and the Wiedemann–Franz law, and lattice thermal conductivity ( $k_{\text{lattice}}$ ) is obtained by subtracting electron thermal conductivity ( $k_{\text{electron}}$ ) from total thermal conductivity ( $k_{\text{total}}$ ). (D) Comparison between inorganic perovskites and other single crystals with ultralow thermal conductivity [Ba<sub>8</sub>Ga<sub>16</sub>Ge<sub>30</sub> (36), Yb<sub>11</sub>InSb<sub>9</sub> (37), Yb<sub>11</sub>Sb<sub>10</sub> (38), La<sub>2</sub>Mo<sub>2</sub>O<sub>9</sub> (39), Yb<sub>14</sub>AlSb<sub>11</sub> (40)]. (Inset) Ratio of lattice thermal conductivity to the minimum thermal conductivity for AIHP NWs.

To elucidate the fundamental mechanisms responsible for the observed ultralow thermal conductivity, we apply a combination of density-functional theory (DFT) and the Boltzmann transport equation (BTE) (details in *SI Appendix*) (31). Considering the intrinsic uncertainty associated with perturbation theory and DFT-based simulations, the calculated  $k_{\text{lattice}}$  values without fitting parameters are in reasonable agreement with the experimental values at high temperature (Fig. 2 A–C). At low temperature, an empirical model is adopted to describe defect and boundary scatterings, and the computed data qualitatively agree with the trend observed in experimental data (Fig. 2 A–C).

Our simulations show that the extremely low  $k_{\text{lattice}}$  can be attributed to low group velocities ( $v_g$ ) and more importantly to extremely short phonon mean-free paths ( $l$ ). The calculated  $v_g$  in all cases is quite small ( $v_g < 2,000 \text{ m s}^{-1}$ ) due to constituent heavy atoms in AIHP (*SI Appendix*, Fig. S9 and Table S3). In general,  $l$  is suppressed by scattering with intrinsic defects and with the NW surface at low temperature, and by phonon–phonon scattering at high temperature (Fig. 3A and *SI Appendix*, Figs. S12 and S13). In AIHP, strong interactions between optical and acoustic modes are stimulated as a result of the large number of band crossings in the low-frequency range (Fig. 3A, *Inset*). Although the  $l$  distribution is much broader and the phonon scattering rates are slightly smaller

in the  $\delta$ -phase than in the  $\gamma$ -phase, these factors in combination with their distinct phonon density of states (DOS) still lead to a similar  $k_{\text{lattice}}$  in both situations (*SI Appendix*, Fig. S10).

Extremely short maximum  $l$  associated with 95% contribution to total  $k_{\text{lattice}}$  ( $\gamma$ -CsSnI<sub>3</sub>: 3.9 nm,  $\gamma$ -CsPbBr<sub>3</sub>: 5.6 nm,  $\delta$ -CsPbI<sub>3</sub>: 14.2 nm) is caused by dramatic anharmonicity due to a cluster rattling mechanism (Fig. 3A). The rattling mechanism associated with local soft modes is widely accepted to be responsible for the low  $k_{\text{lattice}}$  in clathrates (32) and Zn<sub>4</sub>Sb<sub>3</sub> (33). From the cage structure of the  $\gamma$ -phase, it is intuitive to consider the rattling mechanism as the main source of anharmonicity. However, it is nontrivial why such an effect would be especially significant in the  $\gamma$ -phase, and how this concept would extend to the  $\delta$ -phase where there are no explicit cages. To answer these questions, we correlate the rattling strength with structural inhomogeneity via an analysis of bond length distributions. In the case of  $\gamma$ -CsSnI<sub>3</sub> (Fig. 3B), the different distances between the Cs rattler and the surrounding I atoms generates soft optical modes as evidenced by the projected DOS on Cs atoms (*SI Appendix*, Fig. S10). In  $\delta$ -CsPbI<sub>3</sub> (Fig. 3C), although no single atom can be isolated from the network, the inhomogeneous bond length map enables us to identify clusters composed of Pb and I atoms that are loosely bound to their neighbors. These clusters play a similar role as atomic rattlers

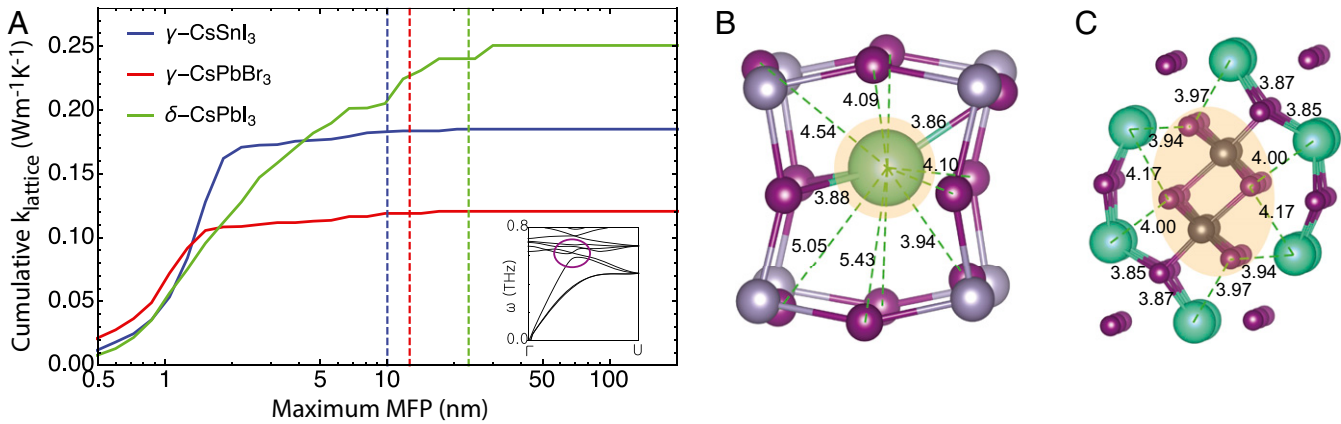


**Fig. 3.** Theoretical analysis of lattice thermal conductivity ( $k_{\text{lattice}}$ ) based on the cluster rattling model. (A) Cumulative  $k_{\text{lattice}}$  with respect to mean-free path ( $l$ ) at room temperature computed by a combination of BTE and DFT, with dashed lines illustrating the defect concentrations fitted to the experimental data shown in Fig. 2. (Inset) Phonon dispersion curve of  $\gamma\text{-CsSnI}_3$  calculated by DFT, with the band crossing between optical and acoustic modes highlighted by the purple circle. (B and C) Inhomogeneous bonding structures associated with (B) atomic and (C) cluster rattling mechanisms in  $\text{CsSnI}_3$  and  $\text{CsPbI}_3$ , respectively. The Cs-I bonds with length  $<3.90 \text{ \AA}$  are shown as sticks, while the others are denoted by dashed lines. The rattling units are highlighted by orange-shaded regions.

but with a larger characteristic size, which is consistent with the dominant contribution from Pb and I atoms to the phonon DOS in the low-frequency range (*SI Appendix*, Figs. S10 and S11), and this explains the longer  $l$  in the  $\delta$ -phase compared with that in the  $\gamma$ -phase as a consequence of the reduced scattering rates between phonons with short wavelengths. Within this framework, we further identified a variety of low-frequency phonon modes that contribute to the cluster rattling mechanism, which are associated with 0D/1D/2D collective motions in both  $\gamma\text{-CsSnI}_3$  and  $\delta\text{-CsPbI}_3$  crystals (*SI Appendix*, Fig. S11).

Since the rattling mechanism has been widely believed to rely on the presence of sufficient interstitial space that enables intensive vibration of rattlers, relevant investigations have been limited to a few types of materials with large cages (34) or layered structures (35). In addition, most of the rattlers reported so far contain only one atom/molecule (34) or components with incoherent motions (35), and the reduction of thermal conductivity was attributed to a single type of rattler. Via quantitative joint experimental-theoretical analysis, we present the unambiguous demonstration of the impact of cluster rattling mechanism on thermal transport properties: comparable and even lower  $k_{\text{lattice}}$  of

AIHPs compared with HHPs (18) ( $k_{\text{HHP}} = 0.5 \text{ W}\cdot\text{m}^{-1}\cdot\text{K}^{-1}$ ) imply that the strength of phonon-phonon scattering induced by the cluster rattling mechanism is comparable to that originating from the individual rattlers. While the size, shape, symmetry, and vibrational modes of the organic molecule are key parameters for thermal transport properties in HHP (20), the topological pattern and bond strength distribution of the entire framework dictates thermal transport properties in AIHP.

To understand other transport properties of  $\text{CsSnI}_3$ , we measured the four-probe electrical conductivity ( $\sigma$ ) and Seebeck coefficient ( $S$ ) of the exact same NW studied for thermal transport in Fig. 2C with the suspended microisland devices (Fig. 4A). At room temperature,  $\sigma$  is  $282 \text{ S}/\text{cm}$  and  $S$  is  $79 \mu\text{V}/\text{K}$ . Temperature-dependent  $\sigma$  exhibits metallic behavior, and the positive sign of  $S$  indicates a hole-dominant (*p*-type) semiconductor, in agreement with previous studies (24). We also performed experiments on several single  $\text{CsSnI}_3$  NWs, and the results are consistent (*SI Appendix*, Fig. S8). Remarkably,  $\text{CsSnI}_3$  NWs have a relatively high electrical conductivity, yet ultralow thermal conductivity ( $k_{\text{total}} = 0.57 \text{ W}\cdot\text{m}^{-1}\cdot\text{K}^{-1}$  at 300 K). We also estimated the hole mobility ( $\mu$ ). Electronic relaxation time is extracted by fitting the calculated  $\sigma$  to experimental

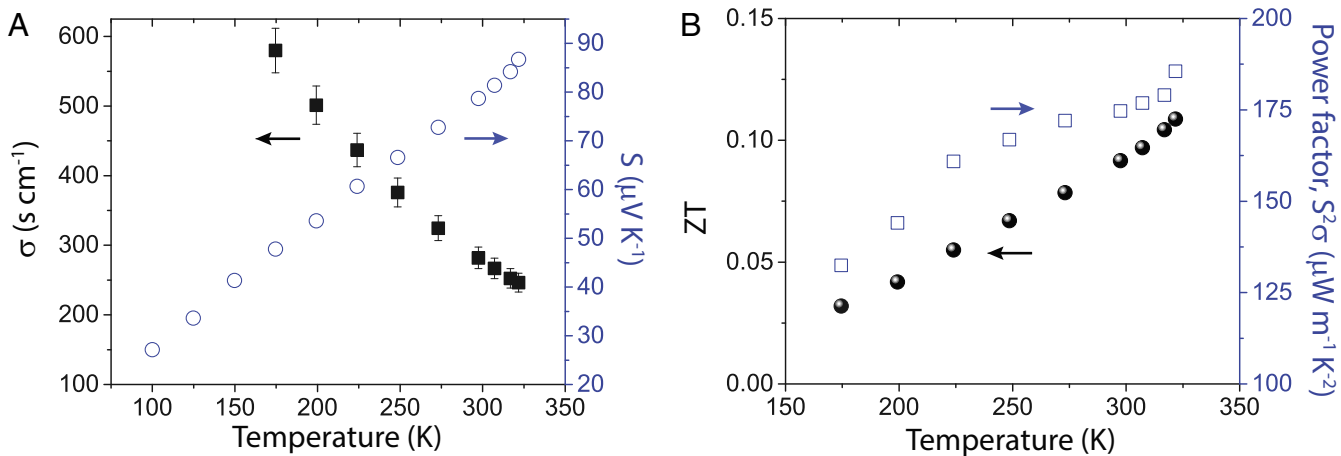


**Fig. 4.** Experimental data of thermoelectric properties in  $\text{CsSnI}_3$ . (A) Temperature-dependent electrical conductivity ( $\sigma$ , black squares) and Seebeck coefficient ( $S$ , blue circles) of a single  $\text{CsSnI}_3$  NW, which is the exact same NW studied in Fig. 2C. The positive sign of  $S$  indicates *p*-type behavior, and  $\text{CsSnI}_3$  exhibits a relatively high electrical conductivity despite its ultralow thermal conductivity. (B) Figure of merit  $ZT$  (black dots) and power factor (blue squares) obtained from the exact same single  $\text{CsSnI}_3$  NW studied in Fig. 2C. Power factor and  $ZT$  of as-synthesized  $\text{CsSnI}_3$  before any attempts at optimization are  $186 \mu\text{W}\cdot\text{m}^{-1}\cdot\text{K}^{-2}$  and 0.11 at 320 K, respectively.

data, and a high hole-mobility value of  $394 \text{ cm}^2 \cdot \text{V}^{-1} \cdot \text{s}^{-1}$  at room temperature is obtained from  $\sigma = ne\mu$  in the low concentration limit, with the carrier concentration estimated by fitting the calculated Seebeck coefficient to the experimental data (theoretical analyses of charge transport in AIHP are discussed in detail in *SI Appendix*, Figs. S15–S17). We also report the power factor and  $ZT$  of as-synthesized  $\text{CsSnI}_3$  before any attempts at optimization,  $186 \text{ } \mu\text{W} \cdot \text{m}^{-1} \cdot \text{K}^{-2}$  and 0.11 at 320 K, respectively (Fig. 4B and *SI Appendix*, S8D). We note that electrical conductivity, Seebeck coefficient, and thermal conductivity are measured from the exact same  $\text{CsSnI}_3$  NW, and these values are used to obtain the power factor and  $ZT$ . Data for two other  $\text{CsSnI}_3$  NWs are presented in *SI Appendix*, Fig. S8 and the results are consistent.

Our work reveals that single-crystalline AIHP NWs synthesized by facile low-temperature solution processes have ultralow  $k_{\text{lattice}}$ , and  $\text{CsSnI}_3$  uniquely also possesses high electrical conductivity. Ultralow  $k_{\text{lattice}}$  in AIHP calls attention to the vital thermal transport processes and thermal management strategies needed for the viable development of applications such as phononic devices, thermoelectric devices, optoelectronic devices, and electrically conductive thermal barrier coatings. Further, the generality of the cluster rattling mechanism will provide insights to discover other inorganic crystals with ultralow thermal conductivity.

## Materials and Methods

Additional details regarding the materials and methods may be found in the *SI Appendix*.

**Synthesis of  $\gamma$ - $\text{CsSnI}_3$  NWs.** A saturated solution of CsI (99.99%, anhydrous beads, Aldrich) in anhydrous methanol (99.8%, Spectrum) is prepared by allowing the solution to stir for at least 1 h. Afterward, clean Si or  $\text{SiO}_2$  substrates ( $1 \text{ cm}^2$ ) are heated to 100 °C and are allowed to equilibrate for 10 min. The saturated CsI solution (70  $\mu\text{L}$ ) is pipetted dropwise onto the substrates without spilling, and the solution is allowed to completely dry for 30 min. Afterward, the CsI-coated substrates are placed in a 20-mL vial

(Kimble, F574504-20) with the CsI-coated side facing up. The vial containing the CsI-coated substrates is heated to 60 °C before the reaction begins.

Separately, a saturated stock solution of  $\text{SnI}_2$  (99.99%, ultradry, Alfa Aesar) in anhydrous 2-propanol (99.5%, Aldrich) is prepared (6.6 mmol/L) by stirring overnight, and the solution is diluted with anhydrous 2-propanol to 4.03 mmol/L. To begin the reaction, 1 mL of  $\text{SnI}_2$ /2-propanol solution is pipetted onto the CsI-coated substrates, and the vial is capped and allowed to react for 90–120 min.

Afterward, the chip is lifted out of the solution, quickly washed in anhydrous 2-propanol, and dried. Our synthesis is performed in an argon-filled glove box with an  $\text{O}_2$  level of <0.1 ppm and an  $\text{H}_2\text{O}$  level of <2.0 ppm.

**Thermal Conductivity Measurement.** The thermal conductivity measurement is based on a well-established single-NW thermometry technique (26), in which microislands are suspended from a substrate to force heat flux through an NW. Two symmetric island structures are each equipped with Pt electrodes, which can act as both a thermometer and a heater, and these islands are supported by thin and long  $\text{SiN}_x$  beams. Individual NWs are placed across the two islands by a manipulator such that the NW bridges the two islands. The NW is then mechanically and thermally anchored on the Pt electrode by electron beam-induced deposition of Pt-C. Subsequently, the single NW on the device is transferred to a closed cycle He cryostat (Janis). Under a high vacuum (<10<sup>-6</sup> torr), one island is heated, and the bridged NW transports heat by conduction to the other island. During this process, the temperature of each island is monitored simultaneously. Knowing the temperature of each membrane and the amount of heat dissipation, the thermal conductance of a single NW can be quantified. The dimensions of the NW are measured using SEM, and the thermal conductivity is calculated using the obtained dimensions.

**ACKNOWLEDGMENTS.** This work was supported by the US Department of Energy, Office of Science, Basic Energy Sciences, Materials Sciences and Engineering Division under Contract DE-AC02-05-CH11231 (Physical Chemistry of Inorganic Nanostructures Program KC3103). Device fabrication was supported by the Laboratory Directed Research and Development Program of Lawrence Berkeley National Laboratory under US Department of Energy Contract DE-AC02-05CH11231. Work at the Molecular Foundry was supported by the Office of Science, Office of Basic Energy Sciences, Materials Sciences and Engineering Division, of the US Department of Energy under Contract DE-AC02-05CH11231. A.B.W. acknowledges the support of the Lam Research Fellowship. D.Z., M.L., and Q.K. acknowledge graduate fellowship from Suzhou Industrial Park.

1. Cahill DG, et al. (2014) Nanoscale thermal transport. II. 2003–2012. *Appl Phys Rev* 1:011305.
2. Goodson KE (2007) Materials science. Ordering up the minimum thermal conductivity of solids. *Science* 315:342–343.
3. Snyder GJ, Toberer ES (2008) Complex thermoelectric materials. *Nat Mater* 7:105–114.
4. Toberer ES, Zevalkink A, Snyder GJ (2011) Phonon engineering through crystal chemistry. *J Mater Chem* 21:15843–15852.
5. Balandin AA (2011) Thermal properties of graphene and nanostructured carbon materials. *Nat Mater* 10:569–581.
6. Cahill DG, Watson SK, Pohl RO (1992) Lower limit to the thermal conductivity of disordered crystals. *Phys Rev B* 46:6131–6140.
7. Zhao L-D, et al. (2016) Ultrahigh power factor and thermoelectric performance in hole-doped single-crystal SnSe. *Science* 351:141–144.
8. Toberer ES, et al. (2008) Traversing the metal-insulator transition in a Zintl phase: Rational enhancement of thermoelectric efficiency in  $\text{Yb}_{14}\text{Mn}_{1-x}\text{Al}_x\text{Sb}_{11}$ . *Adv Funct Mater* 18:2795–2800.
9. Nolas GS, Poon J, Kanatzidis M (2006) Recent developments in bulk thermoelectric materials. *MRS Bull* 31:199–205.
10. Chiriteescu C, et al. (2007) Ultralow thermal conductivity in disordered, layered WSe<sub>2</sub> crystals. *Science* 315:351–353.
11. Ravichandran J, et al. (2014) Crossover from incoherent to coherent phonon scattering in epitaxial oxide superlattices. *Nat Mater* 13:168–172.
12. McMeekin DP, et al. (2016) A mixed-cation lead mixed-halide perovskite absorber for tandem solar cells. *Science* 351:151–155.
13. Chung I, Lee B, He J, Chang RPH, Kanatzidis MG (2012) All-solid-state dye-sensitized solar cells with high efficiency. *Nature* 485:486–489.
14. Tan Z-K, et al. (2014) Bright light-emitting diodes based on organometal halide perovskite. *Nat Nanotechnol* 9:687–692.
15. Hong W-L, et al. (2016) Efficient low-temperature solution-processed lead-free perovskite infrared light-emitting diodes. *Adv Mater* 28:8029–8036.
16. Zhu H, et al. (2015) Lead halide perovskite nanowire lasers with low lasing thresholds and high quality factors. *Nat Mater* 14:636–642.
17. Eaton SW, et al. (2016) Lasing in robust cesium lead halide perovskite nanowires. *Proc Natl Acad Sci USA* 113:1993–1998.
18. Pisoni A, et al. (2014) Ultra-low thermal conductivity in organic-inorganic hybrid perovskite  $\text{CH}_3\text{NH}_3\text{PbI}_3$ . *J Phys Chem Lett* 5:2488–2492.
19. Guo Z, Yoon SJ, Manser JS, Kamat PV, Luo T (2016) Structural phase- and degradation-dependent thermal conductivity of  $\text{CH}_3\text{NH}_3\text{PbI}_3$  perovskite thin films. *J Phys Chem C* 120:6394–6401.
20. Hata T, Giorgi G, Yamashita K (2016) The effects of the organic-inorganic interactions on the thermal transport properties of  $\text{CH}_3\text{NH}_3\text{PbI}_3$ . *Nano Lett* 16:2749–2753.
21. Yue S-Y, Zhang X, Qin G, Yang J, Hu M (2016) Insight into the collective vibrational modes driving ultralow thermal conductivity of perovskite solar cells. *Phys Rev B* 94:115427.
22. Qian X, Gu X, Yang R (2016) Lattice thermal conductivity of organic-inorganic hybrid perovskite  $\text{CH}_3\text{NH}_3\text{PbI}_3$ . *Appl Phys Lett* 108:063902.
23. Zhang D, Eaton SW, Yu Y, Dou L, Yang P (2015) Solution-phase synthesis of cesium lead halide perovskite nanowires. *J Am Chem Soc* 137:9230–9233.
24. Chung I, et al. (2012)  $\text{CsSnI}_3$ : Semiconductor or metal? High electrical conductivity and strong near-infrared photoluminescence from a single material. High hole mobility and phase-transitions. *J Am Chem Soc* 134:8579–8587.
25. Stoumpos CC, Malliakas CD, Kanatzidis MG (2013) Semiconducting tin and lead iodide perovskites with organic cations: Phase transitions, high mobilities, and near-infrared photoluminescent properties. *Inorg Chem* 52:9019–9038.
26. Lee J, et al. (2016) Thermal transport in silicon nanowires at high temperature up to 700 K. *Nano Lett* 16:4133–4140.
27. Lu X, Chu JH, Shen WZ (2003) Modification of the lattice thermal conductivity in semiconductor rectangular nanowires. *J Appl Phys* 93:1219–1229.
28. Beekman M, Morelli DT, Nolas GS (2015) Better thermoelectrics through glass-like crystals. *Nat Mater* 14:1182–1185.
29. Takabatake T, Suekuni K, Nakayama T, Kaneshita E (2014) Phonon-glass electron-crystal thermoelectric clathrates: Experiments and theory. *Rev Mod Phys* 86:669–716.
30. Zhou JS, Goodenough JB (2006) Unusual evolution of the magnetic interactions versus structural distortions in  $\text{RMnO}_3$  perovskites. *Phys Rev Lett* 96:247202.
31. Li W, Carrete JA, Katcho N, Mingo N (2014) ShengBTE: A solver of the Boltzmann transport equation for phonons. *Comput Phys Commun* 185:1747–1758.
32. Dong J, Sankey OF, Myles CW (2001) Theoretical study of the lattice thermal conductivity in Ge framework semiconductors. *Phys Rev Lett* 86:2361–2364.
33. Schweika W, Hermann RP, Prager M, Persson J, Keppens V (2007) Dumbbell rattling in thermoelectric zinc antimony. *Phys Rev Lett* 99:125501.
34. Christensen M, et al. (2008) Avoided crossing of rattler modes in thermoelectric materials. *Nat Mater* 7:811–815.
35. Voneshen DJ, et al. (2013) Suppression of thermal conductivity by rattling modes in thermoelectric sodium cobaltate. *Nat Mater* 12:1028–1032.
36. May AF, Toberer ES, Saramat A, Snyder GJ (2009) Characterization and analysis of thermoelectric transport in n-type  $\text{Ba}_x\text{Ga}_{16-x}\text{Ge}_{30+x}$ . *Phys Rev B* 80:125205.
37. Yi T, Cox CA, Toberer ES, Snyder GJ, Kauzlarich SM (2010) High-temperature transport properties of the Zintl phases  $\text{Yb}_1\text{GaSb}_9$  and  $\text{Yb}_{11}\text{InSb}_9$ . *Chem Mater* 22:935–941.
38. Brown SR, Kauzlarich SM, Gascoin F, Jeffrey Snyder G (2007) High-temperature thermoelectric studies of  $\text{A}_{11}\text{Sb}_{10}$  ( $\text{A}=\text{Yb}, \text{Ca}$ ). *J Solid State Chem* 180:1414–1420.
39. Winter MR, Clarke DR (2007) Oxide materials with low thermal conductivity. *J Am Ceram Soc* 90:533–540.
40. Cox CA, et al. (2009) Structure, heat capacity, and high-temperature thermal properties of  $\text{Yb}_{14}\text{Mn}_{1-x}\text{Al}_x\text{Sb}_{11}$ . *Chem Mater* 21:1354–1360.